JGR Solid Earth

RESEARCH ARTICLE
10.1029/2019JB018335

Quantification of 3-D Thermal Anomalies From Surface Observations of an Orogenic Geothermal System (Grimsel Pass, Swiss Alps)

Christoph Wanner[1], **Larryn W. Diamond**[1], **and Peter Alt-Epping**[1]

[1]Rock-Water Interaction Group, Institute of Geological Sciences, University of Bern, Bern, Switzerland

Key Points:
- Quantification of the heat anomaly below an orogenic geothermal system, combining geochemical observations with numerical simulations
- Calibrated simulations yield large thermal anomalies of 10^2–10^3 PJ per km depth
- Amagmatic orogens are surprisingly promising plays for geothermal power production

Correspondence to:
C. Wanner,
wanner@geo.unibe.ch

Citation:
Wanner, C., Diamond, L. W., & Alt-Epping, P. (2019). Quantification of 3-D thermal anomalies from surface observations of an orogenic geothermal system (Grimsel Pass, Swiss Alps). *Journal of Geophysical Research: Solid Earth*, *124*. https://doi.org/10.1029/2019JB018335

Received 8 JUL 2019
Accepted 17 SEP 2019
Accepted article online 16 OCT 2019

Abstract Geothermal systems in amagmatic orogens involve topography-driven infiltration of meteoric water up to 10 km deep into regional-scale faults and exfiltration of the heated water in surface springs. The thermal anomalies along the upflow zones have not been quantified, yet they are key to estimating the geothermal exploitation potential of such systems. Here we quantify the three-dimensional heat anomaly below the orogenic geothermal system at Grimsel Pass, Swiss Alps, where warm springs emanate from an exhumed, fossil hydrothermal zone. We use discharge rates and temperatures of the springs, temperature measurements along a shallow tunnel, and the formation temperature and depth of the fossil system to constrain coupled thermal–hydraulic numerical simulations of the upflow zone. The simulations reveal that upflow rates act as a first-order control on the temperature distribution and that the site is underlain by an ellipsoidal thermal plume enclosing 10^2–10^3 PJ of anomalous heat per km depth. When the fossil system was active (3.3 Ma), the thermal plume was double its present size, corresponding to a theoretical petrothermal power output of 30–220 MW, with the 120 °C threshold for geothermal electricity production situated at less than 2-km depth. We conclude that mountainous orogenic belts without igneous activity and even with only low background geothermal gradients typical of waning orogens are surprisingly promising plays for petrothermal power production. Our study implies exploration should focus on major valley floors because there the hydraulic head gradients and thus upflow rates and heat anomalies reach maximum values.

1. Introduction

Mountainous orogenic belts without recent igneous activity have been hitherto recognized as plays for geothermal power production only because of the deep sedimentary sequences in their foreland basins, which may host high-enthalpy aquifer-hydrothermal resources (Moeck, 2014). However, the mountain ranges themselves also host geothermal activity, evidenced by thermal springs discharging at temperatures ≤80 °C. These apparently low-enthalpy systems are mostly due to deep circulation of meteoric water through major faults, driven by topographically induced hydraulic head gradients. Examples are in the Canadian Rocky Mountains (Grasby et al., 2016; Grasby & Hutcheon, 2001), the Southern Alps of New Zealand (Menzies et al., 2014; Reyes, 2015; Reyes et al., 2010), the central European Alps (Pfeifer et al., 1992; Sonney & Vuataz, 2008, 2009, 2010), Taiwan (Upton et al., 2011), and the Himalayas (Craw et al., 2005; Hochstein & Yang, 1995). As part of the global search for renewable electricity sources, attention is being paid to these "orogenic geothermal systems" not just because of their water-borne heat but also because of the petrothermal heat deposited by conduction in the low-permeability host rocks around their upflow zones.

Meteoric water that circulates through amagmatic orogens can acquire heat only from the crystalline bedrock. The depth of water penetration therefore determines the maximum reservoir temperature attainable at the base of the system. Several approaches have been taken to assess the penetration depth. In exhumed fossil systems, $\delta^{18}O$ and $\delta^{2}H$ analyses of hydrothermal minerals and fluid inclusions combined with petrological calculations and structural arguments suggest infiltration depths in the range of 5–23 km (Barker et al., 2000; Butler et al., 1997; Cartwright & Buick, 1999; Craw, 1997; Jenkin et al., 1994; McCaig et al., 1990; Menzies et al., 2014; Mulch et al., 2004; Nesbitt et al., 1989; Sharp et al., 2005; Upton et al., 1995; Wickham et al., 1993), implying deep reservoir temperatures up to 400–600 °C (Mulch et al., 2004; Upton et al., 1995). In contrast, classical solute geothermometry applied to analyses of hot springs in orogenic

belts usually reveal reservoir temperatures below 150 °C, such as in the Canadian Rocky Mountains (Grasby et al., 2016), the Qilian Mountains in China (Stober et al., 2016), the Pyrenees in Spain (Asta et al., 2010), and the Swiss Alps (Sonney & Vuataz, 2009). Higher reservoir temperatures are found where extreme uplift rates elevate local geothermal gradients (e.g., Alpine Fault, New Zealand, Reyes et al., 2010; Sutherland et al., 2017) or where deep-sourced, nonmeteoric fluids advect heat upon ascent (e.g., Newell et al., 2015). Considering geothermal gradients typical of waning orogens (25–30 °C/km), the reservoir temperatures in meteoric-dominated systems suggest penetration of meteoric water to less than 6-km depth. Recently, Diamond et al. (2018) took an alternative geochemical modeling approach to determine the penetration depth of meteoric water at the Grimsel Pass geothermal site in the Swiss Alps. The compositions of the thermal waters discharging at that site could be matched by performing forward reactive-transport simulations that treat thermodynamic and kinetic processes of mineral dissolution and precipitation along the upflow path. By combining the calculated 250 °C minimum temperature of water–rock equilibration along the deep flow path with the current geothermal gradient of 25 °C/km, this approach confirmed a penetration depth of at least 10 km (Diamond et al., 2018), thereby bridging the results obtained by classic solute geothermometry and petrologic studies.

Water penetration depths of 10 km or more along even a normal orogenic geothermal gradient (e.g., 25 °C/km) can clearly create a thermal plume well above the ~120 °C threshold required to produce electricity. However, except for the estimates of heat recoverable from aqueous fluids in low-enthalpy geothermal systems in New Zealand (Reyes, 2015), little is known regarding the heat anomalies generated by orogenic geothermal systems. This presents a challenge for assessing their exploitation potential as a renewable energy option in regions unendowed with classic aquifer-hydrothermal resources. Important, but unresolved, questions include (i) what are the shapes, dimensions and magnitudes of their deep thermal anomalies in 3-D? (ii) Is there enough heat in the rocks around the fault-hosted upflow zones to permit petrothermal power production? (iii) How sensitive is the resulting thermal anomaly to the penetration depth of meteoric water along the recharge path?

Here, building on the site parameters derived in the case study of Diamond et al. (2018), we present coupled thermal–hydraulic numerical simulations of the Grimsel Pass orogenic geothermal system in the central Swiss Alps. The main aims of these simulations are to (i) quantify the shape, dimensions and magnitude of the 3-D subsurface thermal anomaly around its upflow zone and (ii) to elucidate its governing parameters. Grimsel Pass is favorable for this treatment because it provides both active and exhumed fossil evidence of geothermal activity in the form of warm springs and hydrothermal breccia outcrops. Together, these yield unique insights into the temporal and spatial evolution of the deep heat plume. To constrain our simulations we have combined numerous surface and near-surface observations made on the current geothermal system (e.g., discharge rates and temperature of warm springs, temperature along a shallow tunnel) with those made on the fossil hydrothermal breccia (e.g., inferred depth and temperature of formation). This permits the magnitude and 3-D geometry of the deep subsurface thermal anomaly to be quantified exclusively from direct near-surface observations.

2. Site Description

Grimsel Pass, which lies between the Rhone and Aare Valleys in the Swiss Alps, is the site of several warm springs that emanate at low flow rates (1–4 L/min) and that have temperatures up to 28 °C (Pfeifer et al., 1992; Waber et al., 2017). Fossil geothermal activity at the same site is expressed by hydrothermal alteration of Pliocene (3.3 Ma) age within the Grimsel Breccia Fault (Hofmann et al., 2004). The present-day springs discharge at an altitude of 1,900–1,915 m above sea level into a N–S trending tunnel ~250 m beneath Grimsel Pass, which hosts a trans-European pipeline for natural gas (hereafter referred to as the Transitgas tunnel after the company who built it in 1973; Figure 1). Grimsel Pass is the lowest point along an E–W profile through the local mountainous topography, but, owing to its saddle shape, it is simultaneously the highest point in a N–S profile between the Aare and Rhone valleys. The warm springs are therefore remarkable because they discharge at the high pass, rather than in the adjacent valleys.

Several studies have already characterized the springs and the fossil geothermal activity, as summarized in the following. The thermal waters have relatively reduced redox states ($Eh_{Ag/AgCl} = -250$ to 10 mV), and chemically they are of Ca–Mg-poor, Na–SO_4–HCO_3 type, carrying up to 280 mg/L total dissolved solids (TDS;

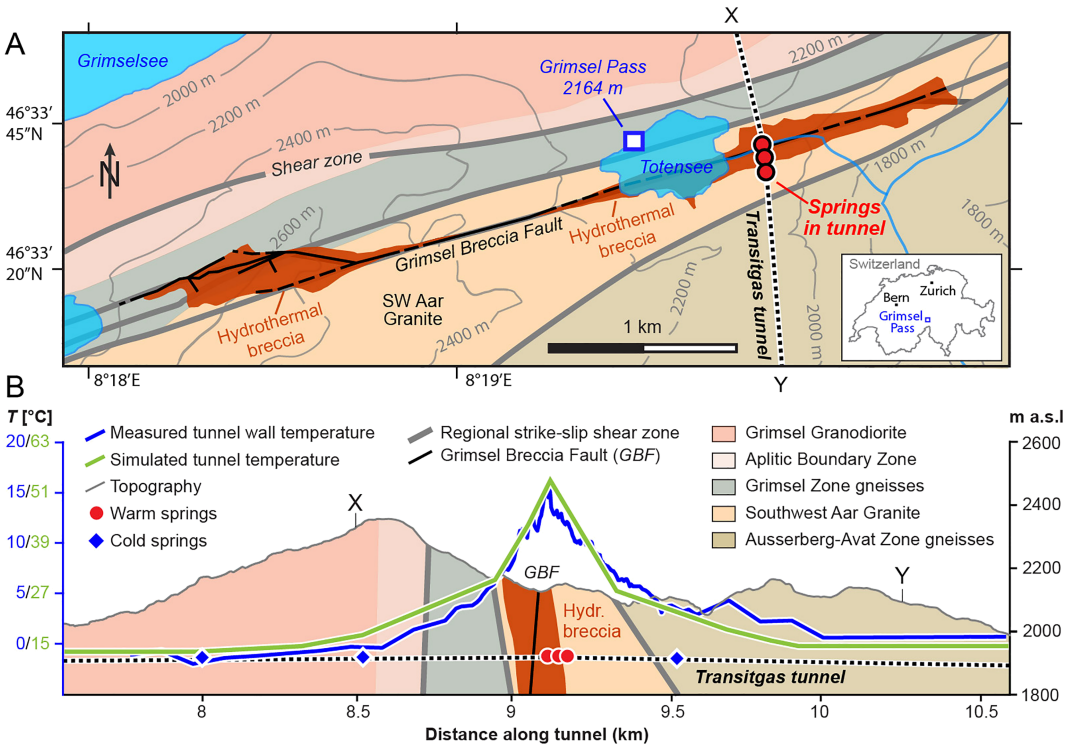

Figure 1. (a) Geological map with Transitgas pipeline tunnel illustrating spatial coincidence between currently active warm springs, regional strike-slip faults, and 3.3-Ma hydrothermally cemented fault-breccias (after Belgrano et al., 2016). (b) Geological cross section along tunnel showing localities of warm springs (>20 °C, circles), cold springs (<20 °C, diamonds), measured tunnel-wall temperature profile (blue; from Egli, Baumann, et al., 2018), and simulated profile (green; this study). The two profiles are plotted at different temperature scales (left *y* axis) to show that our model captures the width of the observed temperature anomaly, whereas the absolute temperatures differ.

Pfeifer et al., 1992; Waber et al., 2017). These properties and their elevated SiO_2, Na, K, Li and F contents, contrast with nearby cold springs, which are poorly mineralized (TDS < 110 mg/L) and of oxidized, Ca–HCO_3 character.

All the thermal springs contain ^{3}H (bomb tritium); thus, they represent mixtures between an old, deeply circulated geothermal end-member that is ^{3}H-free, and a young, cold-water end-member that is ^{3}H-bearing. In the warm spring with the highest solute concentration, the measured ^{3}H activity defines a mixing ratio of about 1:1 (Diamond et al., 2018). Combining this ratio with the ^{14}C concentration shows that the deep geothermal end-member is ^{14}C-free and therefore more than 30 ka old (Waber et al., 2017).

The δ^2H and δ^{18}O values of the thermal springs fall on the local meteoric water line and are well within the range of current rainfall, demonstrating that meteoric water is recharging the geothermal system and that recharge must have occurred at times where the climatic conditions were similar to those of today (Waber et al., 2017). The >30 ka age points to the Middle Würmian interstadial period (which correlates with Marine Oxygen Isotope Stage MIS-3) or to even older warm interglacial periods when significant meteoric recharge was feasible (Dzikowski et al., 2016).

The thermal springs show more negative δ^2H and δ^{18}O values than the nearby cold-water springs, suggesting that the ultimate source of the thermal water is from a distant meteoric infiltration site at a higher altitude than that of Grimsel Pass (Waber et al., 2017). For example, the −15.1‰ δ^{18}O value of the reconstructed end-member thermal water reported by Diamond et al. (2018) is 1.7‰ lower than present surface water (Schotterer et al., 2010). As the local climate during the Middle Würmian MIS-3 or previous interglacial periods was similar to the present (Preusser et al., 2003; Preusser et al., 2011; Spötl & Mangini, 2002), today's δ^{18}H–elevation correlation of −2‰/km in the Grimsel region (Schotterer et al., 2010) can be used to estimate a paleo-infiltration site up to 850 m above Grimsel Pass. Thus, a topographically induced hydraulic head gradient is interpreted to be the main hydraulic force driving ascent of the geothermal water from depth.

Reactive-transport modeling, constrained by the mineralogy of the Pliocene hydrothermally altered breccia, shows that the infiltrating meteoric water reaches a temperature of at least 211 °C and more likely on the order of 230–250 °C along the deepest reaches of its flow path (Diamond et al., 2018).

The Transitgas tunnel crosscuts various steeply dipping crystalline rock units of the Aar Massif (Pfeifer et al., 1992; Figure 1) but the warm springs occur only along a short (<100 m) section of the tunnel where it traverses the Grimsel Breccia Fault. Despite the limited occurrence of warm springs, the tunnel wall shows anomalously high temperatures ($\Delta T = T - T_{\text{background}} \leqslant 16$ °C) along a tunnel section of about 1 km (Egli, Baumann, et al., 2018), suggesting that heat transport is not only occurring by convection along the hydraulically active part of the Grimsel Breccia Fault but also by conduction into the less fractured part of the Aar Massif. The porous, water-conducting Grimsel Breccia Fault, which has been examined in a shallow (115-m depth) research borehole (Egli, Baumann, et al., 2018), dips 85° to the NNW, and therefore, it intersects the tunnel almost perpendicularly. The Breccia Fault is a product of brittle reactivation of an older ductile shear zone that belongs to the Grimsel Pass Fault Zone, a dense set of major ENE trending mylonitic faults that show late strike-slip displacement and that extend along strike over tens of kilometers through the Central Alps (Belgrano et al., 2016; Herwegh et al., 2017). The Grimsel Breccia Fault is named after two ~0.25-km^2 zones containing swarms of narrow, mineralized breccias that outcrop over about 4.5 km along strike of the host fault and that have pipe-like forms in 3-D (Figure 1; Belgrano et al., 2016). These permeable breccia pipes focus ascent of the thermal water to high altitude at Grimsel Pass, while flow toward the deep valleys to the north and south is blocked by intact granite and by ENE trending low-permeability mylonites. Drainage along the Breccia Fault toward the ENE, where the fault outcrops at lower altitude than at Grimsel Pass, is blocked by clay-bearing gouge. Thus, structural controls explain the unexpected occurrence of springs on the high mountain pass, rather than in the adjacent valleys (Figure 1a).

The main host rock of the Grimsel Breccia Fault is the Southwest Aar Granite of Variscan age (Berger et al., 2016; Schaltegger, 1990). Its clasts within the breccias are hydrothermally altered and cemented by a mineral assemblage of quartz and adularia with minor chalcedony, clay minerals, and pyrite (Hofmann et al., 2004). The late-stage adularia in the breccia has been dated at 3.3 ± 0.06 Ma (Hofmann et al., 2004). Fission-track and U–Th/He dates in the distal wall rocks (Egli, Glotzbach, et al., 2018; Vernon et al., 2009) combined with the present rock uplift rate of ~0.9 km/Ma (Hofmann et al., 2004) indicate a recent mean denudation rate of ~0.75 km/Ma, implying the currently exhumed breccia lay ~2.5 km below the paleosurface at 3.3 Ma (Diamond et al., 2018). Fluid inclusion homogenization temperatures corrected for 2.5-km hydrostatic pressure indicate the breccia was mineralized at a temperature of at least 165 ± 5 °C (Diamond et al., 2018). Fluid inclusion analyses show the mineralizing fluid had low salinity (0.5 wt % $NaCl_{eq.}$) and temperature-corrected stable-isotope signatures of the hydrothermal minerals reveal that, like the warm springs, the paleo-fluid was of meteoric origin ($\delta^2H = -110$ to -137‰; $\delta^{18}O = -11$ to -7‰; Hofmann et al., 2004).

In the absence of any Pliocene–Pleistocene igneous activity in the Central Alps, the only source of heat for the water circulating through the Grimsel Pass geothermal system is that dictated by the orogenic geothermal gradient in its wall rocks, which has maintained a value of ~25 °C/km over the past 3.3 Ma (Bodmer, 1982; Vernon et al., 2008).

3. Numerical Model

Our thermal–hydraulic model aims to quantify the current thermal structure of the heat anomaly deep below Grimsel Pass. We therefore simulate only the upflow zone of the geothermal system, using available constraints on the hydraulic head gradients and temperature–depth relations to specify the boundary conditions of the model.

3.1. Constraints on Temperature–Depth Relations

Among the features of the site described in section 2, there are four major thermal–hydraulic, near-surface observations to which our simulations can be compared (Figure 2a). For the remainder of the paper these selected observations will be referred to as calibration targets. The values of these targets are presented in the following.

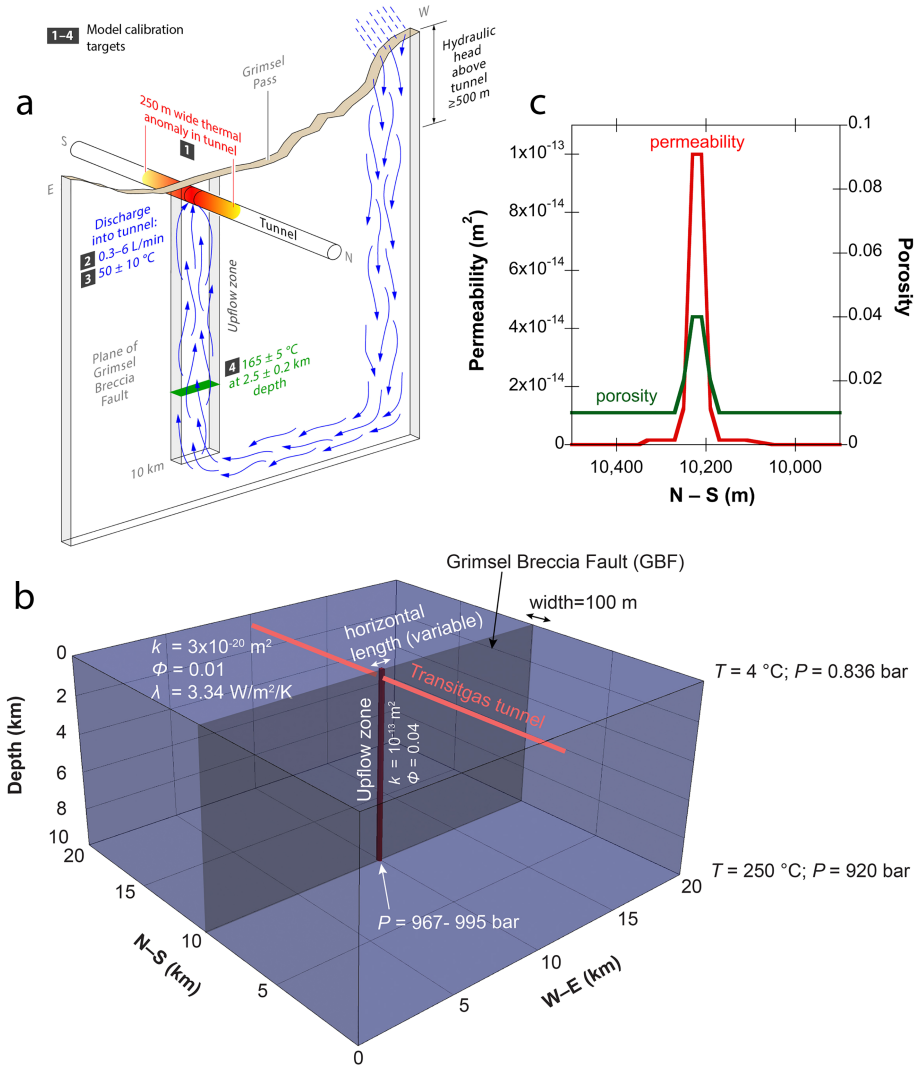

Figure 2. (a) Schematic view (not to scale) of the Grimsel Breccia Fault, the active upflow path of thermal water, and the Transitgas tunnel. Numbers 1–4 show the values of key constraints used as calibration targets for the numerical modeling. Only the upflow segment of the flow path is simulated in this study. (b) Model setup showing the detailed 3-D geometry and the specified initial and boundary conditions for an inferred recharge infiltration depth of 10 km. (c) Specified permeability and porosity profile along the Transitgas tunnel.

3.1.1. Spring Discharge Temperature Within the Transitgas Tunnel

Cooling of the geothermal water upon ascent and mixing with cold surface water results in a discharge temperature of 28 °C. The effect of cold water infiltration on spring temperatures in mountainous terrains depends on several factors: the permeability contrast between hydraulically active fault zones and their surrounding country rocks, the dip angle of the fault zones, and the horizontal distance between the hydraulically active fault zones and the site of surface water infiltration (Ferguson et al., 2009; Forster & Smith, 1989; Lazear, 2006; López & Smith, 1995). Thus, cooling by surface water varies from site to site and for the Grimsel Pass system it is difficult to estimate at which depth and in which geometry this mixing and cooling occurs below the level of the Transitgas tunnel. In the nearby underground Grimsel Test Site, which lies at 450–500-m depth, surface water infiltrates along localized brittle structures but wall-rock temperatures correspond perfectly with those expected from the overburden thickness and the regional geothermal gradient of 25 °C/km (Schneeberger et al., 2017). This suggests that any major cooling by surface water occurs at depths shallower than 500 m. Similarly, in the more distant Gotthard rail base tunnel, which traverses the same crystalline massif as at Grimsel Pass, the effects of cooling by infiltrating meteoric water are observable only along sections of the tunnel with less than 500-m overburden (Rybach & Busslinger, 2013). At Grimsel Pass,

however, surface water could conceivably penetrate deeper into certain zones of the Breccia Fault while thermal water rises up other zones of the same structure. Because we cannot quantify the depth of mixing and because we are primarily interested in the deep thermal structure of the geothermal system, in our model we choose to neglect any cooling due to infiltration of surface water down fractures. This is consistent with previous modeling studies showing that cooling is less significant when upflow is focused within 1D, pipe-like structures (e.g., McKenna & Blackwell, 2004; Taillefer et al., 2017)—which is the case at Grimsel Pass—rather than in planar fault zones that are hydraulically active throughout their 2-D extent (e.g., Dzikowski et al., 2016). Given this assumption, the top ~1 km of our model will represent a hypothetical warm scenario. Therefore, we subtract the effect of near-surface mixing on the spring temperatures by using the mean and standard deviation of the temperature of the unmixed geothermal end-member ($T = 50 \pm 10$ °C) estimated by Diamond et al. (2018). This end-member temperature serves as the first calibration target of our upflow model at 250 m below Grimsel Pass.

3.1.2. Spring Discharge Rates Within the Transitgas Tunnel

The reported total discharge rate of warm springs into the Transitgas tunnel varies between 2 and 8 L/min (Diamond et al., 2018; Pfeifer et al., 1992). Due to the practical difficulties of sampling beneath the gas pipeline, however, the measurement error associated with these rates is conservatively estimated at up to 50%. Moreover, the discharge rates apply to a mixture of deep geothermal fluid and cold surface water. According to Diamond et al. (2018), the cold-water fraction in the warm springs varies from 51 to 70 vol %. Altogether, these considerations yield cold-water corrected discharge rates of the unmixed geothermal fluid of 0.3 to 6 L/min, which serves as the second calibration target in our model at 250 m below Grimsel Pass.

3.1.3. Width of Thermal Anomaly Along Transitgas Tunnel

As evident from the difference between the maximum tunnel wall temperature (16 °C) and the discharge temperatures of the thermal springs (≤28 °C), the tunnel wall temperatures reported by Egli, Baumann, et al. (2018) do not reflect true rock temperatures. The difference is due to several effects. First, most segments of the tunnel wall are covered by a layer of concrete ("shotcrete") with a lower thermal conductivity than the host rocks. Second, cold meteoric water is infiltrating from the surface (at the time of sampling this corresponded to meltwater of final winter snow at ~0 °C; Waber et al., 2017). This inflow is most likely the reason why the variable thickness of rock overburden (0–300 m; Figure 1b) does not seem to influence the tunnel wall temperatures. This interpretation is in agreement with temperature measurements at sites of surface-water influx along the Gotthard rail base tunnel (Rybach & Busslinger, 2013), as explained above. Finally, no attempt was made to correct for the thermal effect of air circulation within the 3-m-diameter, 10.4-km-long tunnel. Because cooling by surface water and air circulation in the tunnel have opposing effects on the width of the temperature anomaly (narrowing versus widening) we believe that, despite the listed artifacts, the temperature profile recorded along the tunnel approximately captures the width of the temperature anomaly induced by the undisturbed geothermal system. Therefore, we take 250 m, corresponding to the length of the tunnel section where the recorded temperature is above half of the observed maximum anomaly ($\Delta T \geq 0.5 \times \Delta T_{max}$, with $\Delta T = T - T_{background}$), as the third calibration target in our model at the tunnel level below Grimsel Pass.

3.1.4. Depth at $T = 165$ °C

A basic premise of our model is that today's thermal springs and the exhumed mineralized breccia at Grimsel Pass belong to the same geothermal system (Hofmann et al., 2004), which has been active, albeit perhaps intermittently, for several million years. All the available information summarized in section 2 is compatible with this premise. Thus, following the approach of Diamond et al. (2018), the paleo-characteristics of the breccia provide us with a window into the subsurface characteristics of the past and possibly into the present-day geothermal activity. Whereas the breccia was mineralized at 2.5 ± 0.2-km depth at 165 ± 5 °C, the background geothermal gradient (25 °C/km) dictates a depth of ~ 6.5 km to heat water to 165 °C. Evidently, advection of heat by the ascending water has raised the 165 °C isotherm by ~ 4 km within the upflow zone, a fact that can be used to constrain our model. Accordingly, we take $T = 165 \pm 5$ °C at 2.5 ± 0.2-km depth as the fourth calibration target within the upflow zone of our model.

3.2. Model Setup

The model was set up as a 3-D cuboid domain (Figure 2b and Table 1) to capture the interplay between three thermal effects: (i) convective heat transport due to fluid flow along the hydraulically active part of

Table 1
Values and Sources of Parameters Used in the Numerical Simulations

Parameter	Value	Source
Dimensions of modeled domain		
N–S and E–W dimensions of total domain	20 × 20 km	Chosen to avoid heat conduction artifacts
Vertical length of total domain	10 km	Depths required to reach a temperature of 250 °C at the background geothermal gradient derived from geochemical modeling (Diamond et al., 2018)
N–S width of upflow zone	100 m	Equal to length of tunnel segment containing warm springs
E–W length of upflow zone	50–150 m	Constrained to less than 4.5-km strike length of breccia
Hydraulic properties		
Hydraulic head driving upflow	500–800 m	Inferred from $\delta^{18}O$ values in Diamond et al. (2018) and from altitude range of present-day topography
Porosity of upflow zone	0.04	Total fracture apertures in borehole
Permeabililty of upflow zone	10^{-13} m^2	Hydraulic tests in upflow zone (Cheng & Renner, 2018)
Porosity of rock outside upflow zone	0.01	He-pycnometry on samples from nearby Grimsel Test Site (Bossart & Mazurek, 1991)
Permeability of rock outside upflow zone	3×10^{-20} m^2	Calculated from hydraulic conductivity determined in nearby Grimsel Test Site (Ota et al., 2003)
Bulk rock density ρ	2660 kg/m^3	Measurements in nearby Grimsel Test Site (Keusen et al., 1989)
Minimum water residence time	30 ka	Waber et al. (2017)
Cold-water corrected discharge rate of thermal water into Transitgas tunnel	0.3–6 L/s	Diamond et al. (2018)
Thermal properties		
Background surface temperature	4 °C	Annual mean
Water discharge temperature in upflow zone	50 ± 10 °C	Mean and standard deviation of geothermal end-member as calculated by Diamond et al. (2018)
Background geothermal gradient	25 °C/km	Vernon et al. (2008)
Steady-state depth at 165 °C in upflow zone	2.5 km	Equal to exhumation depth of 3.3-Ma breccia with formation temperature of 165 ± 5 °C (Diamond et al., 2018)
Thermal conductivity of wet granite	3.34 W m^{-1} K^{-1}	Measurements in nearby Grimsel Test Site (Kuhlmann & Gaus, 2014)
Heat capacity of granite	$C_p = f(T)$	Miao et al. (2014)
Width of temperature anomaly across upflow zone ($\Delta T \geq 0.5 \times \Delta T_{max}$)	250 m	Egli, Baumann, et al. (2018)

the Grimsel Breccia Fault, (ii) conductive heat transport from the underlying deep basement, and (iii) conductive heat loss from the upflow zone into the surrounding rocks of the Aar Massif and to the surface. A large horizontal area of 20 × 20 km was chosen for the model to ensure that heat conduction in the area of interest was not affected by the lateral boundaries of the model. The top of the model domain is flat, without topography and its elevation was set at the altitude of Grimsel Pass (2,164 m above sea level). Thus, the force to drive fluid ascent is given in the model by an appropriate fluid overpressure at the base of the upflow zone (see below). The real topography rises to 500 m above the altitude of the Grimsel Pass some 2.2 km to the west, along the strike of the Grimsel Breccia Fault (and to steadily higher altitudes beyond that, reaching 1,000 m above the pass at 12–14-km distance). We therefore take 500 m as the minimum hydraulic head that drives meteoric water circulation through the system, consistent with the stable isotope constraints (i.e., δ^2H and $\delta^{18}O$ values). The vertical model length was set to 10 km according to the maximum penetration depth of meteoric water estimated by Diamond et al. (2018). To assess the sensitivity of our calibration targets with respect to the penetration depth, however, two additional simulations were run in which the vertical model length was set to 8 and 12 km, respectively.

The hydraulically active upflow zone was placed in the center of the 20 × 20 × 10 km domain and assigned a horizontal N–S width of 100 m, based on the length of the tunnel segment over which the thermal springs occur. Little information is available regarding the horizontal E–W length of the active upflow zone along the Grimsel Breccia Fault (i.e., perpendicular to the tunnel) and indeed there may be other warm springs on the surface outside the tunnel area that are hidden by Quaternary cover. However, the active upflow zone is presumably much shorter than the 4.5-km total length of the breccia bodies. Consequently, multiple simulations were run in which the horizontal E–W length of the active fluid upflow zone was varied between 50 and 150 m.

The Transitgas tunnel was not explicitly defined in the model owing to its small diameter (3 m) and so the simulated tunnel parameters simply correspond to those calculated 250 m below the upper model boundary. Since the tunnel induces a local pressure drop that draws in fluid from the surroundings, we further assume that the current upflow zone is centered on the tunnel (Figure 2b). The entire model domain was discretized into cuboid grid blocks with dimensions of 1 km × 1 km × 200 m in distal regions and decreasing to 1 m × 25 m × 200 m toward the upflow zone, where more detail is required to represent high thermal gradients.

3.3. Initial and Boundary Conditions

The hydraulically active upflow zone was assigned a permeability of 10^{-13} m^2 along the entire vertical extent of the model (Figure 2c and Table 1). This value is based on borehole hydraulic tests performed within the Grimsel Breccia Fault at 90-m depth (Cheng & Renner, 2018). In contrast, the remainder of the model domain was assigned a permeability of 3×10^{-20} m^2 to represent intact granite, in accord with measurements in the nearby underground Grimsel Test Site (Ota et al., 2003). This permeability value ensures that only minor fluid flow occurs outside the upflow zone, consistent with the observed spatial restriction of flow to the breccia body at Grimsel Pass, despite the steep fall of the surface topography to the north, south and southeast of the Pass.

The porosity of the upflow zone was set to 0.04, which corresponds to the total aperture of fractures visible in the televiewer log from the borehole that traverses the Breccia Fault (Egli, Baumann, et al., 2018). The decrease in porosity toward the surrounding rock was set to mimic the observed decrease in spacing and in apertures of fractures mapped across a profile perpendicular to the Breccia Fault (Belgrano et al., 2016). This approach resulted in a linear decrease in porosity to a value of 0.01 outside the upflow zone (Figure 2b), consistent with laboratory measurements of the porosity of the undeformed granite (Bossart & Mazurek, 1991). The corresponding permeability profile was set to follow the cubic law (Witherspoon et al., 1980), assuming that the decrease in porosity is predominantly caused by a decrease in fracture aperture (Figure 2c). The thermal conductivity of the wet rock was set to 3.34 W m^{-1} K^{-1} for the entire model domain based on values reported for the granite within the Grimsel Test Site (Kuhlmann & Gaus, 2014).

Within the model domain we assume an initial hydrostatic pressure distribution and an initial conductive temperature distribution with a geothermal gradient of 25 °C/km. At the four lateral model boundaries, temperature and pressures were fixed to the initially specified values. The upper model boundary was set to 4 °C and 0.836 bar (Figure 2b), whereas at the lower model boundary the initial temperature and pressure depend on the considered penetration depth. For 8 and 10 km, they were set to 200 °C at 745 bar and 250 °C at 920 bar, respectively (Figure 2b), while for a penetration of 12 km the values were set to 300 °C at 1,084 bar. As the altitude of the recharge zone is not known precisely we ran simulations covering a hydraulic head from 500 to 800 m. To do so, the hydrostatic water pressure at the bottom of the upflow zone was varied from 47 to 76 bar to initiate upflow.

3.4. Numerical Simulator

Numerical simulations were performed using TOUGH2 (Pruess et al., 1999), a well-established code for modeling coupled thermo-hydrodynamic processes in geothermal and volcanic systems (e.g., McKenna & Blackwell, 2004; Wanner et al., 2014). All simulations were performed using equation-of-state EOS1, which simulates water flow and coupled heat flow in the single-phase state according to

$$\frac{\partial M_{W,H}}{\partial t} = -\nabla F_{W,H} + q_{W,H} \tag{1}$$

where $M_{W,H}$ is the accumulation term for water M_W (kg/m^3) or heat M_H (J/m^3), $F_{W,H}$ refers to the water flux F_W (kg m^{-2} s^{-1}) or heat flux F_H (J m^{-2} s^{-1}), and $q_{W,H}$ denotes water or heat sinks (−) or sources (+). For fully saturated, single-phase flow problems F_W is equal to the Darcy flux u (m/s)

$$u = -\frac{k}{\mu}(\nabla P - \rho g) \tag{2}$$

where k is the permeability (m^2), μ is the water viscosity (kg m^{-1} s^{-1}), ∇P (Pa m^{-1}) is the water pressure gradient with respect to distance (i.e., hydraulic head gradient), ρ is the density of water (kg/m^3), and g is the gravitational acceleration (m/s^2). Heat flux F_H (J s^{-1} m^{-2}) is defined as

$$F_H = C_M \times T \times \rho_M \times u - \lambda \times \nabla T \quad (3)$$

where C_M (J kg^{-1} K^{-1}) and ρ_M (kg/m^3) are the specific heat capacity and the density of the porous medium (rock + porewater), T (K) is the temperature of the porous medium, λ is the thermal conductivity of the wet rock (J s^{-1} m^{-1} K^{-1} = W m^{-1} K^{-1}), and ∇T (K/m) is the gradient in temperature between adjacent grid blocks. Equation EOS1 calculates the temperature dependence of water properties (e.g., density, specific enthalpy and viscosity) from the Steam Table Equations given by the International-Formulation-Committee (1967).

4. Results and Discussion

4.1. Sensitivity Analysis

Key simulation results are listed in Table 2 for eight different combinations of hydraulic head, horizontal length of the active upflow zone, and meteoric water penetration to illustrate the sensitivity of our calibration targets to the feasible variation in these parameters. Figure 3 illustrates the steady-state temperature distribution for all eight combinations. Increasing the hydraulic head and the horizontal length both increase the temperature within the upflow zone as well as within the adjacent, hydraulically less active part of the Aar Massif. Consequently, this results in increasing tunnel discharge temperatures and widths of the thermal anomaly, while the depth at which the temperature in the upflow zone is 165 °C decreases. This behavior of our calibration targets is observed because both varied parameters affect the amount of hot water infiltrating the system at depth (Figure 2). Whereas increasing the hydraulic head increases upward flux according to Darcy's law (equation (2)), increasing the horizontal length of the upflow zone increases the total fluid injected (in each simulation the area over which the overpressure was defined was increased proportionally to keep the injection rate constant over the entire base of the upflow zone). However, the correlations between the calibration targets and the hydraulic head or the horizontal length of the upflow zone are not fully linear (Table 2). For instance, increasing the hydraulic head from 500 to 650 m at a constant horizontal length of 75 m yields a smaller increase of the simulated discharge temperature in the tunnel (9.4 °C) than when the hydraulic head increases from 650 to 800 m (11.6 °C). Similarly, the temperature increase obtained when increasing the horizontal length from 50 to 100 m (45.3 °C) at a constant head difference of 750 m is smaller than when increasing the length from 100 to 150 m (51.9 °C). This nonlinearity is due to the decrease in fluid density and viscosity with increasing water temperature, and the fact that these fluid properties are important controls on the upflow velocity (equation (2)). This means that the temperature increase initially caused by increasing fluid injection at depth is accelerated by a positive feedback on the flow rate via the temperature dependency of fluid density and viscosity. For instance, the viscosity of pure water decreases from 0.98 to 0.53 g m^{-1} s^{-1} when the temperature increases from 20 to 50 °C, whereas the density decreases from 998.2 to 988.0 kg/m^3. As a consequence, the simulated discharge rate in the tunnel is nearly doubled when increasing the hydraulic head by a factor of only 1.6 (500 to 800 m; Table 2). Likewise, the temperature dependence of fluid viscosity and pressure is the reason why the discharge rate in the tunnel varies for the simulations that were run at a constant hydraulic head of 750 m (Table 2). Since the upflow rate is controlled by the temperature dependence of fluid properties, there is an almost perfect linear correlation between simulated discharge temperatures in the tunnel and total system-wide upflow rates along the hydraulically active part of the host fault (Figure 4). This demonstrates that the total upflow rate is the principal control on the discharge temperature in the tunnel because it is correlated to the amount of heat entering the system at depth.

In contrast to their sensitivity to the hydraulic head and horizontal length of the active upflow zone, our calibration targets are almost insensitive to the variation in penetration depth of meteoric water. This is because conductive heat transport from the upflow zone into the hydraulically inactive part of the surrounding rock mass plays an important role in controlling the temperature distribution of the system in addition to vertical heat advection within the upflow zone. Toward the surface, heat conduction is controlled by the fixed surface temperature of 4 °C. This is the reason why in the model considering 8-km penetration, the 50, 100, and 150 °C isotherms can catch up to those in the models considering deeper penetration (Figure 3a, bottom panel). The importance of heat conduction in controlling the near-surface temperature distribution is also reflected by the weak variation in the simulated width of the thermal anomaly. Thus, the width of the anomaly in the tunnel exhibits the smallest variations among our calibration targets (Table 2). The simulated discharge

Table 2
Observed Versus Simulated Calibration Targets for a Series of Different Combinations of Hydraulic Heads, Horizontal Lengths of the Upflow Zone, and Recharge Penetration Depths

	T_{max}/penetration depth	Hydraulic head (m)	Horizontal length of upflow zone (m)	T_{Tunnel} inflow (°C)[a]	Tunnel discharge rate (kg/min)[b]	Width of T anomaly ($\Delta T \geq 0.5 \times \Delta T_{max}$)	Depth to reach 165 °C (km)	System-wide upflow rate (kg/min)[c]
Observation	≥250 °C/10 km	≥500	?	50 ± 10	0.3–6	250	2.5 ± 0.2	?
Simulations	250 °C/10 km	750	50	28.6	2.5	240	5.6	41.2
		750	100	73.9	4.6	290	3.9	148.7
		750[d]	150	125.8	6.8	350	2.3	321.8
		500	75	29.7	1.9	250	5.5	45.2
		650	75	39.1	2.7	250	5.1	65.8
		800[e]	75	50.7	3.7	260	4.7	90.5
	200 °C/8 km	800[e]	75	53.1	4.0	260	4.9	97.7
	300 °C/12 km	800[e]	75	48.4	3.5	260	4.7	84.7

[a]Steady-state values (Figure 5.) [b]Discharge rate of thermal water integrated over a tunnel section of 100 m and a tunnel diameter of 3 m. [c]Total vertical upflow rate within the entire upflow zone (Figure 2). [d]Model run approximately matching the 165 ± 5 °C formation temperature of the Pliocene breccia at the inferred depth of 2.5 ± 0.2 km. [e]Calibrated models (i.e., best fit with currently observed calibration targets).

temperatures in the tunnel show a minor increase with decreasing penetration depth (Table 2). This is because the hydraulic head gradient driving upflow increases at constant infiltration altitude and decreasing penetration depth.

Similarly to our calibration targets (Table 2), the time required to reach thermal steady state at the simulated tunnel inflow depends on the chosen input parameters and increases with the system-wide upflow rate and hence with increasing discharge temperatures in the tunnel (Figure 5). For the considered parameters it takes up to 10,000 years until full steady-state is reached, although the increase in temperature is negligible after about 2,000 years of continuous, steady-state flow. This is well within the 30-ka minimum time required for each aliquot of meteoric water to flow through the entire recharge–reservoir–discharge path at Grimsel, based on ^{14}C decay (Waber et al., 2017).

4.2. Model Calibration

Our sensitivity analysis has demonstrated that, ignoring cooling effects from surface water infiltration (cf. Forster & Smith, 1989), the temperature distribution of the Grimsel Pass orogenic geothermal system mainly depends on the system-wide fluid upflow rate, which is controlled by the hydraulic head gradient and the extent of the upflow system. Among our various simulations, those that assume a hydraulic head of 800 m and a horizontal length of 75 m successfully reproduce three out of the four calibration targets (Table 2 and Figure 2a). First, the simulated discharge temperatures in the tunnel fall within the temperature range of $T = 50 \pm 10$ °C, as estimated for the unmixed geothermal end-member water (Diamond et al., 2018). Second, the modeled 3.5–4.0-kg/min discharge rates along the 100-m-wide active section of the tunnel fall within the cold-water corrected discharge rates (0.3–6 L/min). Third, the width of the temperature anomaly recorded on the tunnel wall (Egli, Baumann, et al., 2018) is well reconstructed (Table 2), and the simulated tunnel-wall temperature profile reproduces this anomaly almost perfectly (Figure 1b).

In contrast, none of the simulation runs are able to simultaneously reproduce the fourth calibration target derived from the fossil hydrothermal breccia, that is, the 2.5 ± 0.2-km target depth where the temperature in the upflow zone is 165 °C. Instead, the model runs that match the 50 ± 10 °C discharge temperature predict depths between 4.7 and 4.9 km (Table 2). Based on our conclusion that the discharge temperature is directly controlled by the total fluid upflow rate (Figure 4), the discrepancy with respect to the breccia formation depth suggests that upflow rates in the past were higher than today. Our simulations require a system-wide upflow rate of 322 kg/min and hence an increase by a factor of 3.6 to approximately match the 165 °C breccia formation temperature at ~2.5-km depth (Table 2). For such a high upflow rate the predicted, hypothetical paleo-discharge temperature is 126 °C, well above the current value of 50 ± 10 °C. The flow rate and the temperature distribution proposed for the paleo-system are consistent with those of two thermal spas producing from a similar fault-hosted orogenic setting at Brigerbad and Lavey-les-Bains in the nearby Rhone Valley (Sonney & Vuataz, 2008, 2009; Valla et al., 2016). Both sites are currently producing at 700 to 1,200 L/s

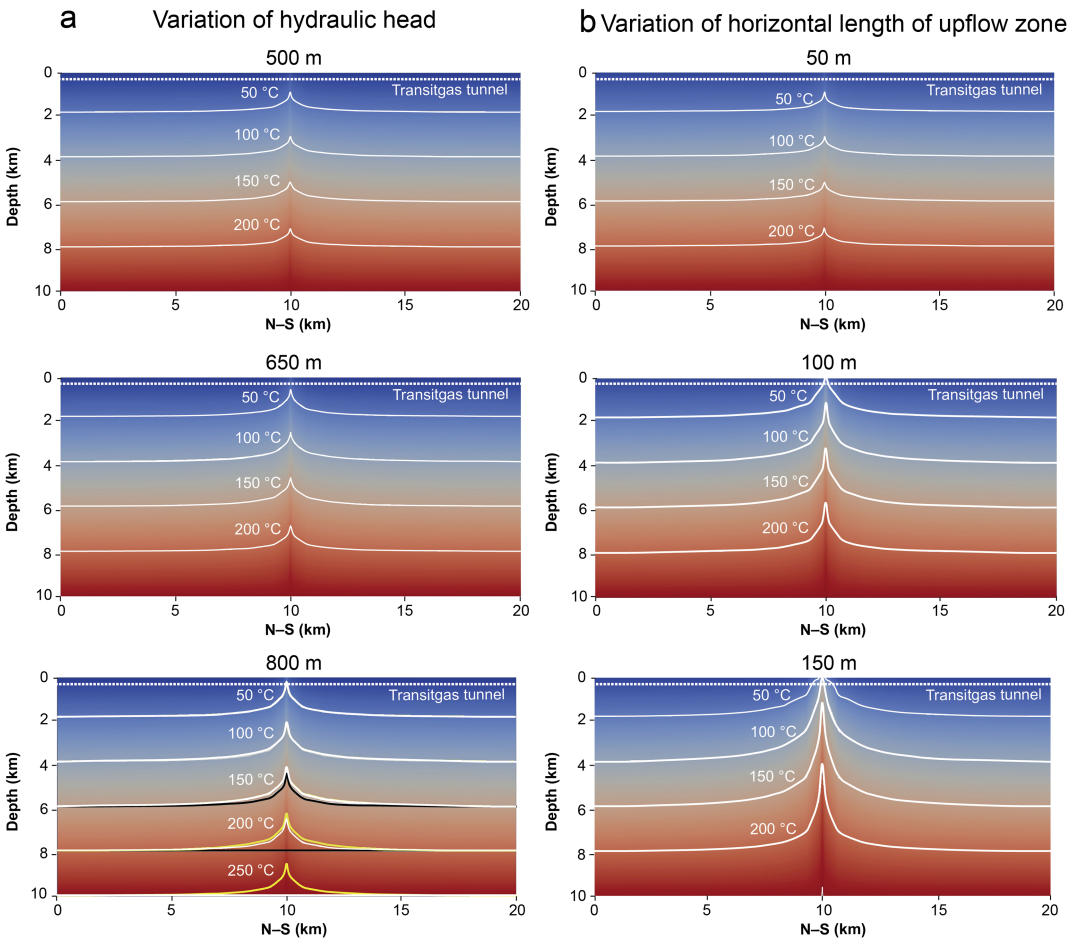

Figure 3. Simulated steady-state temperature distributions for various combinations of hydraulic head and horizontal length of the upflow zone parallel to the Grimsel Breccia Fault for a recharge penetration of 10 km. The panels show the model slice that is perpendicular to the fault and that includes the Transitgas tunnel (Figure 2a). (a) Temperature distribution for constant horizontal length of 75 m and variable hydraulic head. (b) Temperature distribution for constant hydraulic head of 750 m and variable horizontal length of the upflow zone. Note that the bottom panels correspond to the simulations that match observations of (a) the current system and (b) the fossil system. The bottom panel of (a) shows isotherms for penetration depths of 8 km (black), 10 km (white), and 12 km (yellow).

and temperature measurements in shallow boreholes reveal temperatures >100 °C at 1-km depth. Recalling that our model neglects mixing with cold surface water, these values compare well with the 322 kg/min and 126 °C tunnel discharge temperature estimated for the paleo-system at Grimsel Pass (Table 2).

Despite the simultaneous agreement of our model results with three calibration targets, it is impossible to quantify exactly the hydraulic head and the horizontal length of the current upflow system. This is because the model is underconstrained and other combinations of these parameters can equally reproduce the cooling-corrected discharge temperature and discharge rates of the warm springs, as well as the thermal anomaly along the Transitgas tunnel. A similar nonuniqueness applies to permeability variations, which have the same effect on the flow system as variable hydraulic head gradients (equation (2)) and were thus not explicitly explored in our sensitivity analysis. Finally, due to the low sensitivity of the system to the penetration depth of recharging meteoric water (Table 2), our simulations cannot further constrain the maximum penetration depth. Hence, the 10 km postulated by Diamond et al. (2018) remains a minimum value.

4.3. Thermal Anomaly

The simulation results allow us to evaluate the magnitude and 3-D extent of the thermal anomaly induced by the Grimsel Pass geothermal system. To do so, the temperature anomaly ΔT is calculated as the difference between the steady-state temperature distribution of the calibrated models and that corresponding to the natural background (i.e., distal) geothermal gradient. In Figure 6, the anomaly is illustrated for the

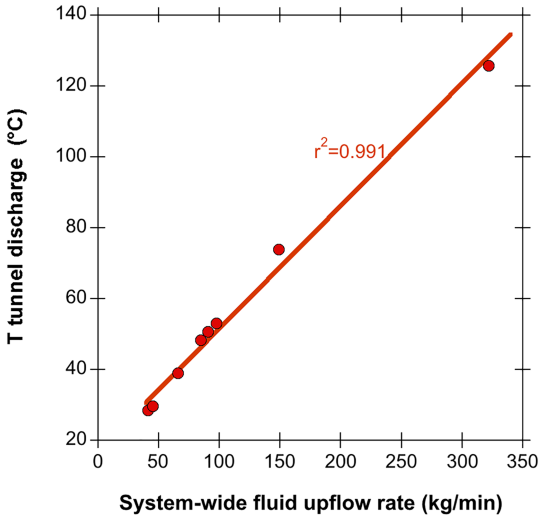

Figure 4. Correlation between simulated tunnel discharge temperatures and system-wide upflow rates, which were varied by running the model with various combinations of hydraulic head and horizontal lengths of the upflow zone (Table 2).

current and fossil systems in terms of a contour surface where $\Delta T = 15$ °C, resulting in vertically elongated ellipsoids. Interestingly, the maximum width of the ellipsoids appears some 4–5 km above the base of the upflow zone in the model. This is because the temperature difference at the lower model boundary is zero (Figure 2) and a certain vertical flow distance is required before ΔT evolves to a steady state. At shallower levels than its maximum width, the thermal anomaly decreases due to conductive cooling toward the 4 °C surface temperature. Similarly to the recorded temperature profile in the tunnel (Figure 1b), the simulated 3-D temperature anomaly is much wider than the actual upflow zone. In reality, however, the magnitude of the anomaly is likely lower in the uppermost kilometer owing to advective cooling by surface water infiltration, which was not considered in our model. In the case of the fossil system, our simulation predicts a maximum horizontal extent of the $\Delta T = 15$ °C anomaly of about 3×3 km (Figure 6b), despite the active upflow zone being limited to 150×100 m.

From the calculated temperature difference ΔT, the anomalous heat H (i.e., the heat in excess of that provided by the background conductive temperature profile) was calculated according to

$$H = \sum_i C_P \times \rho \times V_i \times \Delta T_i \quad (4)$$

where C_p (J kg^{-1} K^{-1}) is the heat capacity of the rock at constant pressure (with a temperature dependency obtained by interpolating heat capacity measurements on a granitic sample similar to the Southwest Aar Granite in Miao et al. (2014), ρ refers to the bulk rock density (2,660 kg/m^3), V_i (m^3) is the volume of grid block i, and ΔT_i (K) denotes the temperature difference between the steady state considering fluid flow and the initial conductive temperature distributions in block i. To calculate the anomalous heat available for an exploitable petrothermal reservoir size, equation (4) was integrated over 1-km depth intervals, resulting in values of 200–3,000 PJ/km (Figure 6).

5. Implications for Exploration for Orogenic Geothermal Systems

The calibrated model indicates that significant thermal anomalies are associated with orogenic spring systems even at low system-wide upflow rates (<100 kg/min), such as in the case of the studied system (Figure 6a). Moreover, the spatial coincidence between fossil and recent hydrothermal manifestations demonstrates that these systems can persist, even if only intermittently, over several million years.

The heat excesses shown in Figure 6 can be converted to theoretical geothermal power outputs by dividing by time and by assuming a thermal recovery factor of 5% (Aravena et al., 2016) during an exploitation period of 20 years. This yields values of 13–94 MW per km depth for the current Grimsel Pass system and 36–222 MW per km depth for the fossil system. Due to the limited extent of the active fluid upflow zone (Figure 2), however, orogenic geothermal systems may need to be stimulated in order to increase the permeability of the hydraulically inactive zones and thereby enable exploitation of their stored heat via doublet-type water circulation. Even though the host faults may be seismically dormant, this step could of course add to the challenge of maintaining induced seismicity at an acceptable level (Bachmann et al., 2011). Moreover, based on the simulated temperature distribution for the current situation at Grimsel Pass (Figure 3a), drilling to a depth of about 3.5 km is required to reach temperatures that allow production of electricity (>120 °C). This inferred depth does not represent a significant benefit versus nominally hot-dry rock systems in central Europe such as at Soultz, France or Basel, Switzerland, where geothermal gradients are somewhat higher at 37–39 °C (Alt-Epping et al., 2013; Genter et al., 2010). Therefore exploration for orogenic hot-spring systems in mountainous terrains should focus on deeply-rooted sites similar to Grimsel Pass, but with higher flow rates. This conclusion follows from our results that high upflow rates increase the 3-D size of the induced thermal anomaly as well as increasing the temperature at a specific depth (Figure 3 and Table 2). Larger and hotter anomalies than the one at Grimsel Pass further ensure a longer exploitation lifetime, which is

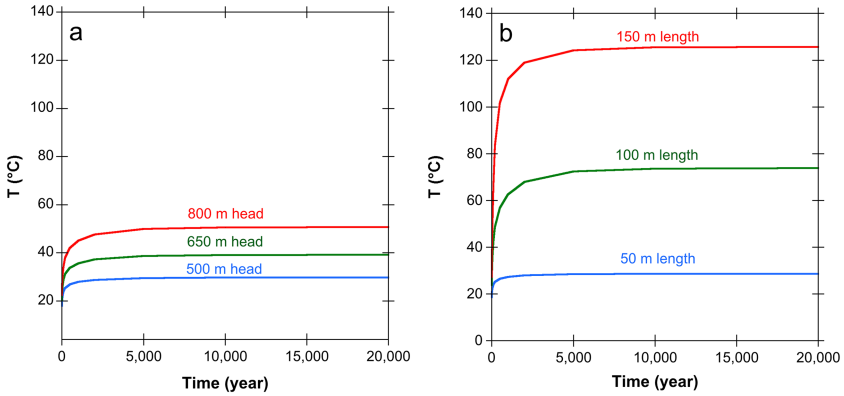

Figure 5. Simulated temporal evolution of discharge temperatures in the tunnel as a function of horizontal length of the upflow zone, hydraulic head, and a fixed recharge penetration depth of 10 km. (a) Horizontal length of 75 m and variable head. (b) Constant hydraulic head of 750 m and variable horizontal length of the upflow zone.

important given that it takes at least several hundred years of undisturbed upflow for such resources to renew (Figure 5).

In the Central Alps, more promising examples of orogenic geothermal systems are present within the same fault-hosted setting at Brigerbad and Lavey-les-Bains in the nearby Rhone Valley (Sonney & Vuataz, 2009; Valla et al., 2016). At both sites, upflow rates and local geothermal gradients are comparable to those revealed by our simulations of the fossil Grimsel Pass system, which implies heat anomalies more than double that of the current Grimsel Pass system (Figure 6 and Table 2). However, according to the systematics inferred from our modeling, the Brigerbad and Lavey-les-Bains sites have higher potential than even the

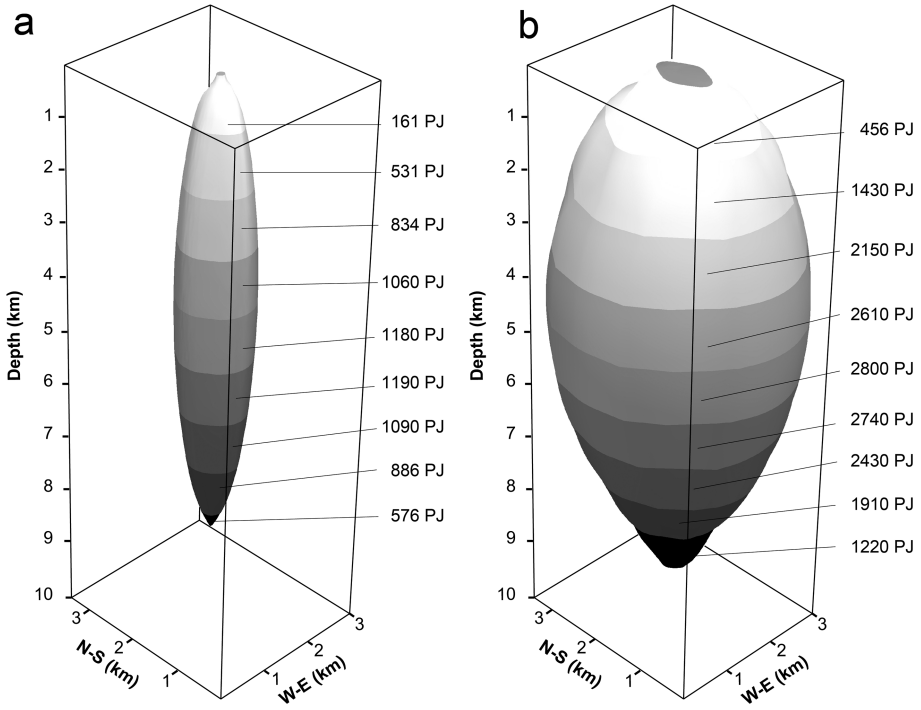

Figure 6. Anomalous heat per km depth calculated for (a) the model calibrated to the current Grimsel Pass hydrothermal system and (b) the model run that reproduces the breccia formation temperature of 165 °C at a depth of ~2.5 km and hence corresponds to the fossil system (Table 2). The shape of the anomalies are illustrated in terms of the $\Delta T = 15$ °C contour surfaces determined from the difference between the steady-state temperature distribution of the calibrated models (Table 2) and the distal background geothermal gradient. Due to their limited extent, the anomalies are shown for a cuboid with a base of 3.5 km × 3 km, located in the center of the total 3-D model domain (Figure 2).

fossil system at Grimsel Pass because they discharge at the valley floor, where hydraulic head gradients and thus upflow rates reach maximum values for a given fault zone permeability and depth of meteoric water penetration. Moreover, the simulations suggest, in accord with the formation temperatures of the mineralized breccias, that the 120 °C isotherm required for electricity production lies at about 2-km depth in such systems (Figure 3b, bottom panel), thereby favoring their accessibility for exploitation.

Finally, based on the observed lack of sensitivity of the shallow temperature anomaly to the penetration depth of recharging meteoric water (Figure 3a, bottom panel), the actual penetration depth does not constitute a key parameter for the exploitation potential of orogenic geothermal systems, as long as the penetration is deep enough to yield temperatures well above the 120 °C threshold for electricity production.

6. Summary and Conclusions

We have developed a new approach to assess the shape, dimensions, and magnitude of the subsurface thermal anomalies in fault-hosted orogenic geothermal systems, which does not rely on deep borehole or geophysical information. This entails combining surface observations of warm springs and fossil hydrothermal mineralization to constrain 3-D thermal–hydraulic numerical modeling. By removing the cooling effect of infiltrating surface water in the top kilometer of the system, our simulations reveal the systematic behavior of the upflow zone: for a fixed length of upflow, hypothetical discharge temperatures as well as the size of the thermal anomaly are controlled by the total, system-wide fluid upflow rate; upflow rates are in turn controlled by the cross section of the hydraulically active fracture zones, their permeability, and the hydraulic head gradient driving the flow. The influence of cold water infiltration into the top of the system will vary from site to site, as has been addressed in previous studies (e.g., Forster & Smith, 1989).

We have calibrated our model against current temperatures and flow rates of thermal springs discharging into a shallow tunnel beneath Grimsel Pass and against the pattern of temperatures along that tunnel wall. This reveals that large ellipsoidal plumes of anomalous heat (10^2–10^3 PJ/km in excess of that dictated by the background geothermal gradient) are generated by orogenic geothermal systems even at low system-wide upflow rates on the order of 100 kg/min. Due to conductive heating of the host rock, these anomalies have much larger footprints than the hydraulically active upflow zones, implying that stimulation measures may be required to exploit them for petrothermal power production. At these low upflow rates, the nominal temperature threshold for electricity production (>120 °C) is not reached at depths shallower than ~3.5 km. However, comparing the calibrated model to the formation temperature of a hydrothermal breccia representing the fossil geothermal system at Grimsel Pass suggests the paleo-system operated at higher flow rates and generated a thermal anomaly about double that of the current system. In this case, the plume corresponds to a theoretical power output of 40–220 MW at 5% recovery and the 120 °C cutoff for electricity production is reached at <2-km depth.

Building on the recent confirmation that meteoric water may penetrate up to 10 km into orogenic faults, our study demonstrates that mountainous orogenic belts without igneous activity and with only low background geothermal gradients (e.g., 25 °C/km) are surprisingly promising plays for petrothermal power production, although renewal rates are on the order of centuries. Our simulations imply that exploration should focus on major valley floors because there the hydraulic head gradients and thus upflow rates and heat anomalies reach maximum values.

Acknowledgments
We thank Transitgas AG for kindly granting access to their pipeline tunnel at Grimsel Pass. Discussions with University of Bern colleagues Thomas Belgrano, Alfons Berger, Daniel Egli, and Marco Herwegh are appreciated. This research was conducted within National Research Programme NRP 70 "Energy Turnaround," funded by Swiss National Science Foundation (SNF) grant 407040_153889 to L.W. Diamond. Geothermal research at the University of Bern is supported by the Swiss Competence Center for Energy Research–Supply for Electricity (SCCER-SoE). Two anonymous reviewers kindly provided constructive comments. All data required to run our simulations and to support our conclusions are provided in the tables and figures of the manuscript, which can also be downloaded at https://doi.org/10.5281/zenodo.3380483.

References

Alt-Epping, P., Diamond, L. W., Häring, M. O., Ladner, F., & Meier, D. B. (2013). Prediction of water–rock interaction and porosity evolution in a granitoid-hosted enhanced geothermal system, using constraints from the 5 km Basel-1 well. *Applied Geochemistry*, *38*, 121–133. https://doi.org/10.1016/j.apgeochem.2013.09.006

Aravena, D., Muñoz, M., Morata, D., Lahsen, A., Parada, M. Á., & Dobson, P. (2016). Assessment of high enthalpy geothermal resources and promising areas of Chile. *Geothermics*, *59*(Part A), 1–13. https://doi.org/10.1016/j.geothermics.2015.09.001

Asta, M. P., Gimeno, M. J., Auqué, L. F., Gómez, J., Acero, P., & Lapuente, P. (2010). Secondary processes determining the pH of alkaline waters in crystalline rock systems. *Chemical Geology*, *276*(1-2), 41–52. https://doi.org/10.1016/j.chemgeo.2010.05.019

Bachmann, C. E., Wiemer, S., Woessner, J., & Hainzl, S. (2011). Statistical analysis of the induced Basel 2006 earthquake sequence: introducing a probability-based monitoring approach for Enhanced Geothermal Systems. *Geophysical Journal International*, *186*(2), 793–807. https://doi.org/10.1111/j.1365-246X.2011.05068.x

Barker, A. J., Bennett, D. G., Boyce, A. J., & Fallick, A. E. (2000). Retrogression by deep infiltration of meteoric fluids into thrust zones during late-orogenic rapid unroofing. *Journal of Metamorphic Geology*, *18*(3), 307–318. https://doi.org/10.1046/j.1525-1314.2000.00257.x

Belgrano, T. M., Herwegh, M., & Berger, A. (2016). Inherited structural controls on fault geometry, architecture and hydrothermal activity: an example from Grimsel Pass, Switzerland. *Swiss Journal of Geosciences*, *109*(3), 345–364. https://doi.org/10.1007/s00015-016-0212-9

Berger, A., Mercolli, I., & Gnos, E. (2016) Geological Map of the Aar Massif, Tavetsch and Gotthard Nappes 1:100000. Landesgeologie der Schweiz.

Bodmer, P. (1982). *Geothermal Map of Switzerland: Schweizerische geophysikalisssche Kommission*. Bern, Switzerland: Kümmerly und Frey.

Bossart, P., & Mazurek, M. (1991). Grimsel Test Site Structural Geology and water flow-paths in the migration shear zone. Nagra Technical Report, NTB 91-12, 1-55.

Butler, R. W. H., Harris, N. B. W., & Whittington, A. G. (1997). Interactions between deformation, magmatism and hydrothermal activity during active crustal thickening; a field example from Nanga Parbat, Pakistan Himalayas. *Mineralogical Magazine*, *61*(404), 37–52. https://doi.org/10.1180/minmag.1997.061.404.05

Cartwright, I., & Buick, I. S. (1999). The flow of surface-derived fluids through Alice Springs age middle-crustal ductile shear zones, Reynolds Range, central Australia. *Journal of Metamorphic Geology*, *17*(4), 397–414. https://doi.org/10.1046/j.1525-1314.1999.00205.x

Cheng, Y., & Renner, J. (2018). Exploratory use of periodic pumping tests for hydraulic characterization of faults. *Geophysical Journal International*, *212*(1), 543–565. https://doi.org/10.1093/gji/ggx390

Craw, D. (1997). Fluid inclusion evidence for geothermal structure beneath the Southern Alps, New Zealand. *New Zealand Journal of Geology and Geophysics*, *40*(1), 43–52. https://doi.org/10.1080/00288306.1997.9514739

Craw, D., Koons, P. O., Zeitler, P. K., & Kidd, W. S. F. (2005). Fluid evolution and thermal structure in the rapidly exhuming gneiss complex of Namche Barwa–Gyala Peri, eastern Himalayan syntaxis. *Journal of Metamorphic Geology*, *23*, 829–845. https://doi.org/10.1111/j.1525-1314.2005.00612.x

Diamond, L. W., Wanner, C., & Waber, H. N. (2018). Penetration depth of meteoric water in orogenic geothermal systems. *Geology*, *46*(12), 1063–1066. https://doi.org/10.1130/G45394.1

Dzikowski, M., Josnin, J. Y., & Roche, N. (2016). Thermal Influence of an Alpine Deep Hydrothermal Fault on the Surrounding Rocks. *Groundwater*, *54*(1), 55–65. https://doi.org/10.1111/gwat.12313

Egli, D., Baumann, R., Küng, S., Berger, A., Baron, L., & Herwegh, M. (2018). Structural characteristics, bulk porosity and evolution of an exhumed long-lived hydrothermal system. *Tectonophysics*, *747-748*, 239–258. https://doi.org/10.1016/j.tecto.2018.10.008

Egli, D., Glotzbach, C., Valla, P. G., Berger, A., & Herwegh, M. (2018). Low temperature thermochronometry (apatite and zircon (U-Th)/He) across an active hydrothermal zone (Grimsel Pass, Swiss Alps). EGU General Assembly 2018, Vienna: Geophysical Research Abstracts, 52, 2749-2765.

Ferguson, G., Grasby, S. E., & Hindle, S. R. (2009). What do aqueous geothermometers really tell us? *Geofluids*, *9*(1), 39–48. https://doi.org/10.1111/j.1468-8123.2008.00237.x

Forster, C., & Smith, L. (1989). The influence of groundwater flow on thermal regimes in mountainous terrain: A model study. *Journal of Geophysical Research*, *94*(B7), 9439–9451. https://doi.org/10.1029/JB094iB07p09439

Genter, A., Goerke, J., Graff, J.-J., Cuenot, N., Krall, G., Schindler, M., & Ravier, G. (2010). Current Status of the EGS Soultz Geothermal Project (France) Paper presented at the World Geothermal Congress, Bali, Indonesia, 25-29 April.

Grasby, S. E., Ferguson, G., Brady, A., Sharp, C., Dunfield, P., & McMechan, M. (2016). Deep groundwater circulation and associated methane leakage in the northern Canadian Rocky Mountains. *Applied Geochemistry*, *68*, 10–18. https://doi.org/10.1016/j.apgeochem.2016.03.004

Grasby, S. E., & Hutcheon, I. (2001). Controls on the distribution of thermal springs in the southern Canadian Cordillera. *Canadian Journal of Earth Sciences*, *38*(3), 427–440. https://doi.org/10.1139/e00-091

Herwegh, M., Berger, A., Baumberger, R., Wehrens, P., & Kissling, E. (2017). Large-scale crustal-block-extrusion during late Alpine collision. *Scientific Reports*, *7*(1), 413. https://doi.org/10.1038/s41598-017-00440-0

Hochstein, M. P., & Yang, Z. (1995). The Himalayan Geothermal Belt (Kashmir, Tibet, West Yunnan). In M. L. Gupta, & M. Yamano (Eds.), *Terrestrial heat flow in geothermal energy in Asia*, (pp. 331–368). New Delhi: Oxford and IBH Publishing.

Hofmann, B. A., Helfer, M., Diamond, L. W., Villa, I. M., Frei, R., & Eikenberg, J. (2004). Topography-driven hydrothermal breccia mineralization of Pliocene age at Grimsel Pass, Aar massif, Central Swiss Alps. *Schweizerische Mineralogische und Petrographische Mitteilungen*, *84*, 271–302. https://doi.org/10.5169/seals-63750

International-Formulation-Committee (1967). *Formulation of the Thermodynamic Properties of Ordinary Water Substance*. Düsseldorf, Germany: IFC Secretariat.

Jenkin, G. R. T., Craw, D., & Fallick, A. E. (1994). Stable isotopic and fluid inclusion evidence for meteoric fluid penetration into an active mountain belt; Alpine Schist, New Zealand. *Journal of Metamorphic Geology*, *12*(4), 429–444. https://doi.org/10.1111/j.1525-1314.1994.tb00033.x

Keusen, H. R., Ganguin, J., Schuler, P., & Buleti, M. (1989). Felslabor Grimsel: Geologie. Nagra. Nagra Technical Report, NTB, 87-14.

Kuhlmann, U., & Gaus, I. (2014). Inverse modelling of the FEBEX in situ test using iTOUGH2. Nagra Arbeitsbericht, NAB 14-20, 1-33.

Lazear, G. D. (2006). Evidence for deep groundwater flow and convective heat transport in mountainous terrain, Delta County, Colorado, USA. *Hydrogeology Journal*, *14*(8), 1582–1598. https://doi.org/10.1007/s10040-006-0058-8

López, D. L., & Smith, L. (1995). Fluid Flow in Fault Zones: Analysis of the Interplay of Convective Circulation and Topographically Driven Groundwater Flow. *Water Resources Research*, *31*(6), 1489–1503. https://doi.org/10.1029/95WR00422

McCaig, A. M., Wickham, S. M., & Taylor, H. P. (1990). Deep fluid circulation in alpine shear zones, Pyrenees, France: field and oxygen isotope studies. *Contributions to Mineralogy and Petrology*, *106*(1), 41–60. https://doi.org/10.1007/bf00306407

McKenna, J. R., & Blackwell, D. D. (2004). Numerical modeling of transient Basin and Range extensional geothermal systems. *Geothermics*, *33*(4), 457–476. https://doi.org/10.1016/j.geothermics.2003.10.001

Menzies, C. D., Teagle, D. A. H., Craw, D., Cox, S. C., Boyce, A. J., Barrie, C. D., & Roberts, S. (2014). Incursion of meteoric waters into the ductile regime in an active orogen. *Earth and Planetary Science Letters*, *399*, 1–13. https://doi.org/10.1016/j.epsl.2014.04.046

Miao, S. Q., Li, H. P., & Chen, G. (2014). Temperature dependence of thermal diffusivity, specific heat capacity, and thermal conductivity for several types of rocks. *Journal of Thermal Analysis and Calorimetry*, *115*(2), 1057–1063. https://doi.org/10.1007/s10973-013-3427-2

Moeck, I. S. (2014). Catalog of geothermal play types based on geologic controls. *Renewable and Sustainable Energy Reviews*, *37*, 867–882. https://doi.org/10.1016/j.rser.2014.05.032

Mulch, A., Teyssier, C., Cosca, M. A., Vanderhaeghe, O., & Vennemann, T. W. (2004). Reconstructing paleoelevation in eroded orogens. *Geology*, *32*, 525–528. https://doi.org/10.1130/g20394.1

Nesbitt, B. E., Muehlenbachs, K., & Murowchick, J. B. (1989). Genetic implications of stable isotope characteristics of mesothermal Au deposits and related Sb and Hg deposits in the Canadian Cordillera. *Economic Geology*, *84*, 1489–1506. https://doi.org/10.2113/gsecongeo.84.6.1489

Newell, D. L., Jessup, M. J., Hilton, D. R., Shaw, C. A., & Hughes, C. A. (2015). Mantle-derived helium in hot springs of the Cordillera Blanca, Peru: Implications for mantle-to-crust fluid transfer in a flat-slab subduction setting. *Chemical Geology*, *417*, 200–209. http://doi.org/10.1016/j.chemgeo.2015.10.003

Ota, K., Möri, A., Alexander, W. R., Frieg, B., & Schild, M. (2003). Influence of the mode of matrix porosity determination on matrix diffusion calculations. *Journal of Contaminant Hydrology*, *61*(1–4), 131–145. https://doi.org/10.1016/S0169-7722(02)00139-0

Pfeifer, H. R., Sanchez, A., & Degueldre, C. (1992). Thermal springs in granitic rocks from the Grimsel Pass (Swiss Alps): The late stage of a hydrothermal system related to Alpine Orogeny. In Y. K. Kharaka, & A. S. Maest (Eds.), *Proceedings of Water-Rock Interaction WRI–7*, (pp. 1327–1330). Park City, Utah: A.A. Balkema, Rotterdam, The Netherlands.

Preusser, F., Geyh, M. A., & Schlüchter, C. (2003). Timing of Late Pleistocene climate change in lowland Switzerland. *Quaternary Science Reviews*, *22*, 1435–1445. https://doi.org/10.1016/S0277-3791(03)00127-6

Preusser, F., Graf, H. R., Keller, O., Krayss, E., & Schlüchter, C. (2011). Quaternary glaciation history of northern Switzerland. *E&G Quaternary Science Journal*, *60*, 282–305. https://doi.org/10.3285/eg.60.2-3.06

Pruess, K., Oldenburg, C., & Moridis, G. (1999). *TOUGH2 users's guide, Version 2.0*, *Rep. LBNL-29400*, (). Berkeley, CA: Lawrence Berkeley National Labortory.

Reyes, A. G. (2015). Low-temperature geothermal reserves in New Zealand. *Geothermics*, *56*, 138–161. https://doi.org/10.1016/j.geothermics.2015.04.004

Reyes, A. G., Christenson, B. W., & Faure, K. (2010). Sources of solutes and heat in low-enthalpy mineral waters and their relation to tectonic setting, New Zealand. *Journal of Volcanology and Geothermal Research*, *192*(3–4), 117–141. https://doi.org/10.1016/j.jvolgeores.2010.02.015

Rybach, L., & Busslinger, A. (2013). Verification of rock temperature prediction along the Gotthard base tunnel - A prospect for coming tunnel projects. Paper presented at the Proceeding World Tunnel Congress 2013 Geneva, Switzerland.

Schaltegger, U. (1990). Post-magmatic resetting of Rb-Sr whole rock ages — a study in the Central Aar Granite (Central Alps, Switzerland). *Geologische Rundschau*, *79*(3), 709–724. https://doi.org/10.1007/BF01879210

Schneeberger, R., Mäder, U. K., & Waber, H. N. (2017). Hydrochemical and Isotopic (δ^2H, δ^{18}O, ^{3}H) Characterization of Fracture Water in Crystalline Rock (Grimsel, Switzerland). *Procedia Earth and Planetary Science*, *17*, 738–741. https://doi.org/10.1016/j.proeps.2016.12.187

Schotterer, U., Schürch, M., Rickli, R., & Stichler, W. (2010). Wasserisotope in der Schweiz - Neue Ergebnisse und Erfahrungen aus dem nationalen Messnetz ISOT. *Gas-Wasser-Abwasser (GWA)*, *12*, 1073–1081.

Sharp, Z. D., Masson, H., & Lucchini, R. (2005). Stable isotope geochemistry and formation mechanisms of quartz veins; Extreme paleoaltitudes of the Central Alps in the Neogene. *American Journal of Science*, *305*, 187–219. https://doi.org/10.2475/ajs.305.3.187

Sonney, R., & Vuataz, F.-D. (2008). Properties of geothermal fluids in Switzerland: A new interactive database. *Geothermics*, *37*(5), 496–509. https://doi.org/10.1016/j.geothermics.2008.07.001

Sonney, R., & Vuataz, F.-D. (2009). Numerical modelling of Alpine deep flow systems: a management and prediction tool for an exploited geothermal reservoir (Lavey-les-Bains, Switzerland). *Hydrogeology Journal*, *17*(3), 601–616. https://doi.org/10.1007/s10040-008-0394-y

Sonney, R., & Vuataz, F.-D. (2010). Remobilisation of deep Na-Cl waters by a regional flow system in the Alps: Case study of Saint-Gervais-les-Bains (France). *Comptes Rendus Geoscience*, *342*(2), 151–161. https://doi.org/10.1016/j.crte.2009.12.011

Spötl, C., & Mangini, A. (2002). Stalagmite from the Austrian Alps reveals Dansgaard-Oeschger events during isotope stage 3: implications for the absolute chronology of Greenland ice cores. *Earth and Planetary Science Letters*, *203*, 507–518. https://doi.org/10.1016/S0012-821X(02)00837-3

Stober, I., Zhong, J., Zhang, L., & Bucher, K. (2016). Deep hydrothermal fluid–rock interaction: the thermal springs of Da Qaidam, China. *Geofluids*, *16*, 711–728. https://doi.org/10.1111/gfl.12190

Sutherland, R., Townend, J., Toy, V., Upton, P., Coussens, J., Allen, M., et al. (2017). Extreme hydrothermal conditions at an active plate-bounding fault. *Nature*, *546*(7656), 137–140. https://doi.org/10.1038/nature22355

Taillefer, A., Soliva, R., Guillou-Frottier, L., Le Goff, E., Martin, G., & Seranne, M. (2017). Fault-Related Controls on Upward Hydrothermal Flow: An Integrated Geological Study of the Têt Fault System, Easter Pyrénées (France). *Geofluids*, *2017*, 1–19. https://doi.org/10.1155/2017/8190109

Upton, P., Craw, D., Yu, B., & Chen, Y.-G. (2011). Controls on fluid flow in transpressive orogens, Taiwan and New Zealand. *Geological Society, London, Special Publications*, *359*(1), 249–265. https://doi.org/10.1144/sp359.14

Upton, P., Koons, P. O., & Chamberlain, C. P. (1995). Penetration of deformation-driven meteoric water into ductile rocks: Isotopic and model observations from the Southern Alps, New Zealand. *New Zealand Journal of Geology and Geophysics*, *38*(4), 535–543. https://doi.org/10.1080/00288306.1995.9514680

Valla, P. G., Rahn, M., Shuster, D. L., & van der Beek, P. A. (2016). Multi-phase late-Neogene exhumation history of the Aar massif, Swiss central Alps. *Terra Nova*, *28*(6), 383–393. https://doi.org/10.1111/ter.12231

Vernon, A. J., van der Beek, P. A., Sinclair, H. D., Persano, C., Foeken, J., & Stuart, F. M. (2009). Variable late Neogene exhumation of the central European Alps: Low-temperature thermochronology from the Aar Massif, Switzerland, and the Lepontine Dome, Italy. *Tectonics*, *28*, TC5004. https://doi.org/10.1029/2008TC002387

Vernon, A. J., van der Beek, P. A., Sinclair, H. D., & Rahn, M. K. (2008). Increase in late Neogene denudation of the European Alps confirmed by analysis of a fission-track thermochronology database. *Earth and Planetary Science Letters*, *270*(3–4), 316–329. https://doi.org/10.1016/j.epsl.2008.03.053

Waber, H. N., Schneeberger, R., Mäder, U. K., & Wanner, C. (2017). Constraints on evolution and residence time of geothermal water in granitic rocks at Grimsel (Switzerland). *Procedia Earth and Planetary Science*, *17*, 774–777. https://doi.org/10.1016/j.proeps.2017.01.026

Wanner, C., Peiffer, L., Sonnenthal, E., Spycher, N., Iovenitti, J., & Kennedy, B. M. (2014). Reactive transport modeling of the Dixie Valley geothermal area: Insights on flow and geothermometry. *Geothermics*, *51*, 130–141. https://doi.org/10.1016/j.geothermics.2013.12.003

Wickham, S. M., Peters, M. T., Fricke, H. C., & O'Neil, J. R. (1993). Identification of magmatic and meteoric fluid sources and upward- and downward-moving infiltration fronts in a metamorphic core complex. *Geology*, *21*(1), 81–84. https://doi.org/10.1130/0091-7613(1993)021<0081:IOMAMF>2.3.CO;2

Witherspoon, P. A., Wang, J. S. Y., Iwai, K., & Gale, J. E. (1980). Validity of cubic law for fluid-flow in a deformable rock fracture. *Water Resources Research*, *16*(6), 1016–1024. https://doi.org/10.1029/WR016i006p01016